



Enhanced photocatalytic hydrogen evolution by partially replaced corner-site C atom with P in g-C₃N₄

Bin Wang^a, Hairui Cai^a, Daming Zhao^b, Miao Song^c, Penghui Guo^b, Shaohua Shen^b, Dongsheng Li^{c,*}, Shengchun Yang^{a,*}

^a School of Science, MOE Key Laboratory for Non-equilibrium Synthesis and Modulation of Condensed Matter, State Key Laboratory for Mechanical Behavior of Materials, Xi'an Jiaotong University, Xi'an 710049, China

^b International Research Center for Renewable Energy (IRCRES), State Key Laboratory of Multiphase Flow in Power Engineering (MFPE), Xi'an Jiaotong University (XJTU), 28 West Xianning Road, Xi'an 710049, China

^c Physical and Computational Sciences Directorate, Pacific Northwest National Laboratory, Richland, WA 99352, United States

ARTICLE INFO

Keywords:

g-C₃N₄
Surface phosphorization
Photocatalysis
Hydrogen evolution
Solar energy

ABSTRACT

Modifying the structure of photocatalyst to tune its electronic and physicochemical properties is an effective approach for efficient photocatalysis. Herein, we modify the structure of g-C₃N₄ by partially replacing the corner site C atom with P heteroatom via a simple thermal phosphorization method. Comparing with the pristine g-C₃N₄, the g-C₃N₄ after phosphorization shows an improved photocatalytic hydrogen activity, which is attributed to the narrowed bandgap and the upshifted conduction band edge, enhanced separation and transfer of photogenerated charges, and highly hydrophilic surface absorbing reactant molecule for photocatalysis. Various experimental characterizations are conducted to systematically explore the underlying essential mechanism behind the superior photocatalytic performance of g-C₃N₄ with phosphorization treatment. This work provides a simple approach to modifying the structure of g-C₃N₄, which could be applied to other semiconductors for designing photocatalyst with unique structure and enhanced activity.

1. Introduction

Hydrogen evolution from water via photocatalysis, a simulating natural photosynthesis process, could attractively convert solar energy into chemical energy, and is a promising method to address the unprecedented increasing demands for energy and environment all over the world [1–8]. Although many efforts have been continuously made to construct a visible light-active photocatalytic system for decades, high efficient conversion of solar energy to hydrogen energy is still challenging. The key to this technology is to design and develop low-cost and environmental friendly photocatalysts with strong light absorption, rapid separation of photo-induced charge carriers, and fast photocatalytic redox reaction on its surface.

Up to now, various semiconductors have been developed as catalysts for photocatalytic hydrogen evolution from water. Among them, graphitic carbon nitride (g-C₃N₄), as a new generation metal-free photocatalyst, has attracted tremendous attention due to its low cost, environmental friendliness, and high stability [9–11]. However, g-C₃N₄ still suffers from low photocatalytic performance due to some obstacles, such as insufficient visible light absorption and rapid recombination of

charge carriers. A lot of efforts have been devoted to obtaining high photocatalytic activities including elemental doping, tailoring its morphologies with unique structures, and constructing type II composites or Z-scheme system with other photocatalysts etc [6,12–21].

Among these various strategies, introducing heteroatoms into g-C₃N₄ framework could distinctly tune its band structure, significantly expand its visible-light response range, and lead to higher photocatalytic activities. For example, Tian et al. reported that Fe doped g-C₃N₄ showed expanded optical absorption to long wavelengths with increasing Fe content [22]. Apart from metal element doping, non-metal elements, such as O, C, S, I, F, have also been introduced into the framework of g-C₃N₄ to modify its optical and electronic properties [23–25]. Huang et al. found the bandgap of O-doped g-C₃N₄ decreased dramatically upon O doping [24]. Dong et al. reported that C atoms could substitute the bridging N atoms in g-C₃N₄, causing the narrowed band gap from 2.72 to 2.65 eV [25].

Apart from traditional doping strategy, the electronic structure of g-C₃N₄ could also be altered by post-treatment in a different atmosphere [26–33], such as H₂, H₂S or NH₃ etc. Zhou et al. found that some structural defects and disorders could be introduced into g-C₃N₄ by

* Corresponding authors.

E-mail addresses: dongsheng.li2@pnnl.gov (D. Li), ysch1209@xjtu.edu.cn (S. Yang).

<https://doi.org/10.1016/j.apcatb.2018.10.044>

Received 9 July 2018; Received in revised form 14 October 2018; Accepted 18 October 2018

Available online 22 October 2018

0926-3373/ © 2018 Elsevier B.V. All rights reserved.

hydrogenation treatment in 3 MPa H₂ at 500 °C. The hydrogenated g-C₃N₄ showed enhanced photocatalytic activity for hydrogen evolution from water by 45% [27]. Liu and co-workers reported the homogeneous substitution of sulfur for lattice nitrogen in C₃N₄ via post-calcining under H₂S environment [34]. Cui et al. synthesized a novel g-C₃N₄ with low defects in the NH₃ atmosphere. This NH₃-treated g-C₃N₄ exhibited well-condensed crystallinity and improved in-plane conjugated network with decreased sp² N defects in heptazine heterocycle, contributing to its superior photocatalytic activity [35].

In this work, we proposed a simple method to tune the structure of g-C₃N₄ by post thermal phosphorization treatment under an inert atmosphere containing PH₃, which is in-situ generated by the disproportionation reaction of thermal decomposing NaH₂PO₂ [36]. The wet grinding mixing g-C₃N₄ and NaH₂PO₂ enabled homogenous and direct reaction of PH₃ and g-C₃N₄. Surface modified g-C₃N₄ with enhanced hydrogen photocatalytic activity was obtained by the proposed phosphorization treatment. The underlying essential mechanism for the enhanced photocatalytic activity was systemically explored in detail.

2. Experimental section

2.1. Chemicals and materials

Urea (CO(NH₂)₂), Sodium hypophosphite (NaH₂PO₂·H₂O), Triethanolamine ((HOCH₂CH₂)₃N, TEOA) are purchased from Sinopharm Chemical Reagent Co., Ltd. Chloroplatinic acid (H₂PtCl₆·6H₂O) is offered by Alfa Aesar, A Johnson Matthey Company. All the materials were analytical grade and used without further purification. The water used in all syntheses was deionized water with a resistivity of 18.25 MΩ·cm.

2.2. Preparation of g-C₃N₄ sample

In brief, 50 g of urea was heated to 550 °C for 4 h in an air atmosphere with a heating rate of 5 °C/min. The resultant yellow product milled into powder in a mortar was g-C₃N₄ sample.

2.3. Phosphorization of g-C₃N₄

Phosphorization of g-C₃N₄ was performed in a tube furnace at 400 °C under N₂ atmosphere. Typically, by adding 500 μL deionized H₂O, 100 mg g-C₃N₄ and 50 mg NaH₂PO₂·H₂O were mixed in an agate mortar and ground for 60 mins via a wet-grinding process. At first, the mixture became a slurry. NaH₂PO₂·H₂O was dissolved during the wet-grinding process, and could be mixed with g-C₃N₄ at the molecular level. Gradually, the deionized H₂O was evaporated along with the continuous grinding process. Finally, the mixed slurry became a wet-solid mixture. The wet-solid mixture was headed in a tube furnace at 400 °C for 120 mins under N₂ atmosphere with a heating rate of 5 °C/min. After cooling, the samples were sonicated in water and ethanol, centrifuged for several times, respectively, and dried under vacuum at 60 °C for 8 h. The obtained was the phosphorized g-C₃N₄, designated as g-C₃N₄(P).

2.4. Photocatalytic reaction

Photocatalytic reactions of hydrogen production from water were conducted in a gas-closed system with a side irradiation Pyrex cell. 12.5 mg of photocatalyst powder was dispersed into 80 mL of 10 vol% triethanolamine solution by sonication for 30 mins. After the reactor was evacuated and refilled with N₂ gas, the suspension was irradiated by visible light (λ ≥ 420 nm) through a cutoff filter from a 300 W Xe lamp for 4 h. The amount of H₂ gas was determined using online thermal conductivity detector (TCD) gas chromatography (NaX zeolite column, TCD detector, N₂ carrier). For photocatalytic hydrogen evolution, 1 wt% Pt as cocatalysts were loaded onto the surface of the as-

prepared photocatalysts by an in-situ photo-deposition method, with an appropriate amount of H₂PtCl₆·6H₂O as Pt precursor. The apparent quantum efficiencies were measured under visible light irradiation with various wavelengths (λ = 420 ± 10 nm, 435 ± 10 nm, 450 ± 10 nm, 500 ± 10 nm, 520 ± 10 nm), and were calculated as defined by Eq. (1):

$$AQE = \frac{\text{The number of evolved hydrogen molecules} \times 2}{\text{The number of incident photons}} \times 100\% \quad (1)$$

2.5. Characterization

The X-ray diffraction (XRD) patterns were obtained from a PANalytical X'pert MPD Pro diffractometer operated at 40 kV and 40 mA using Ni-filtered Cu Kα irradiation (Wavelength 1.5406 Å). UV-vis absorption spectra (UV-vis) were measured on a Hitachi U4100 instrument equipped with labsphere diffuse reflectance accessory using BaSO₄ as the reference. A JSM-7800F instrument (JEOL) was used to perform field emission scanning electron microscopy (FE-SEM). The transmission electron microscopy (TEM) images and scanning transmission electron microscopy (STEM) images were obtained from an FEI Tecnai G2 F30 S-Twin transmission electron microscope at an accelerating voltage of 300 kV. An OXFORDMAX-80 energy-dispersive X-ray detector (EDX) which was mounted in the above TEM was used to conduct the elemental analysis. N₂ adsorption-desorption isotherms were conducted at 77 K using an Accelerated Surface Area and Porosimetry Analyzer (ASAP 2020, Micromeritics) after degassing the samples at 150 °C for 2 h. Surface area was determined using the Brunauer–Emmett–Teller (BET) methods. X-ray photoelectron spectroscopy (XPS) measurements were conducted on a Kratos spectrometer (AXIS Ultra DLD) with monochromatic Al Kα radiation (hν = 1486.69 eV). All binding energies were referenced to the C 1s peak at 284.8 eV. Fourier transform infrared (FTIR) spectra were recorded on a Bruker Vextex 70 FTIR spectrometer using the KBr pellet technique. The photovoltage (SPV) spectra were obtained by using a surface photovoltage spectroscopy. The measurement system consists of a source of monochromatic light (Omni-λ300), a lock-in amplifier (SR830) with a light chopper (SR540), and a sample chamber. Electron paramagnetic resonance (EPR) were obtained by a X-band spectrometer (Bruker EMX, A300-9.5/12/S-LC, Germany) at room temperature. The total P contents in the real sample was analyzed by Inductively Coupled Plasma Mass Spectrometer (ICP-MS) (NexION™ 350D, PerkinElmer, USA). PL spectra (including PL emission and time-resolved PL decay) were carried out at room temperature using a PTI QM-4 fluorescence spectrophotometer. In detail, PL emission spectra were obtained at excitation wavelength of 337 nm, the time-resolved PL decay spectra were observed at 460 nm. For the decay kinetics calculation methods: the value of the goodness-of-fit parameter (χ²) calculated from the tri-exponential decay kinetics method is much closer to 1, which indicates a good fit of the data. Thus, the emission signals were analyzed by the tri-exponential kinetics method rather than other (mono-, bi-, or tetra-exponential) kinetics method. Equations (2) and (3) were applied to carry out the tri-exponential kinetic analysis and to calculate average lifetime τ_{avg}, respectively:

$$\gamma = \sum a_i e^{-\left(\frac{t}{\tau_i}\right)} (i = 1, 2, 3) \quad (2)$$

$$\tau_{avg} = \frac{\sum a_i \tau_i^2}{\sum a_i \tau_i} (i = 1, 2, 3) \quad (3)$$

The kinetic parameters of the time resolved fluorescence emission decay analysis were shown in Table S4 in the Supporting Information.

2.6. Photoelectrode preparation

According to the procedure reported previously [23], the g-C₃N₄ samples were deposited on a carbon cloth substrate via electrophoretic

deposition. Typically, 50 mg of g-C₃N₄ sample was suspended in a 50 mL acetone solution containing 11.25 mg I₂ under ultrasonic treatment. One FTO transparent conductive glass substrate and one carbon cloths (1 × 1.5 cm²) were parallel immersed in the solution at the applied potential of 10 V for 20 min. The g-C₃N₄-coated area was fixed ca. 1 × 1 cm². Then, the deposited electrode was dried at 120 °C for 30 min to remove I₂ residues.

2.7. Photoelectrochemical and electrochemical characterization

Photoelectrochemical and electrochemical measurements were carried out in a conventional three-electrode system. A platinum foil was used as the counter electrode. A saturated calomel electrode (SCE) was used as the reference electrode. An aqueous solution of 0.5 M Na₂SO₄ solution containing 10 vol% TEOA was used as the electrolyte. Photocurrent densities were measured by a CHI 760 scanning potentiostat (CHI Instruments). The scanning rate was 5 mV s⁻¹. A 300 W xenon lamp coupled with a cutoff filter ($\lambda \geq 420$ nm) was used as the light source. The potential, against an SCE (saturated calomel electrode) reference electrode, was converted to the RHE (reversible hydrogen potential) potential using the formula $V_{\text{RHE}} = V_{\text{SCE}} + 0.059 \text{ pH} + 0.2415 \text{ V}$, where V_{RHE} is a potential versus a reversible hydrogen potential, V_{SCE} is the potential versus SCE, and pH is the pH value of the electrolyte.

3. Results and discussion

It is well known that extending the light absorption spectra for photocatalyst could increase the number of photoinduced charge carriers for the photocatalytic reaction. The g-C₃N₄(P) is obtained by post thermal calcination of the mixture of g-C₃N₄ and NaH₂PO₂, i.e. surface phosphorization, and shows an additional absorption band ranging from ~460 to ~650 nm (Fig. 1a) besides the absorption below ~400 nm in contrast to g-C₃N₄, indicating the decrease of its band gap after surface phosphorization. The influence of phosphorization on g-C₃N₄ could also be reflected by the color change from light yellow for pristine g-C₃N₄ to brown for g-C₃N₄(P) (inset of Fig. 1a). Based on the corresponding spectra in Fig. 1a, the band gaps of g-C₃N₄ and g-C₃N₄(P)

are measured by Kubelka–Munk function [37]. A straight line can be obtained in the plot of $(F(R_{\infty})h\nu)^{1/2}$ (as ordinate) vs. $h\nu$ (as abscissa) and the extrapolation of the straight line to $(F(R_{\infty})h\nu)^{1/2} = 0$ axis gives the value of the band gap of the sample, as shown in Fig. 1b. The intrinsic bandgap decreased from ~2.70 eV to 2.52 eV because of phosphorization on g-C₃N₄. The valence band maximum (VBM) edge potential of g-C₃N₄ and g-C₃N₄(P) are measured to be ~2.20 eV and ~1.62 eV by valence band XPS (Fig. 1c), respectively, revealing the slight change of VBM edge of g-C₃N₄ after phosphorization. Combined with the results of Uv–vis spectra, the conduction band edge potential of g-C₃N₄(P) is estimated to be -0.9 V, which is more negative than that of g-C₃N₄ (-0.5 V) (Fig. 1d). It implies that the phosphorization treatment of g-C₃N₄ could not only expand its light absorption spectra but also up-shift the conduction band edge of g-C₃N₄ enabling it thermodynamically favorable for photocatalytic hydrogen reaction.

XRD was used to study the influence of phosphorization on the crystal structure of g-C₃N₄. As displayed in Fig. 2a, g-C₃N₄(P) exhibits two diffraction peaks of (100) and (002), which are consistent with bulk g-C₃N₄ (JCPDS 87–1526), indicating that the original crystal structure of g-C₃N₄ is mainly retained after phosphorization. The FT-IR spectra of g-C₃N₄ and g-C₃N₄(P) in Fig. 2b provides molecular structural information. Several bands located in the 1200–1600 cm⁻¹ region are related to the typical stretching modes of aromatic C–N heterocycles. The peak at ca. 807 cm⁻¹ represents tri-s-triazine unit mode. The bands in the range of 1200–1700 cm⁻¹ belong to the typical stretching vibration of C–N heterocycles. The broad band at 3000–3500 cm⁻¹ are assigned to uncondensed terminal amino groups (–NH₂ or =NH groups) [38]. However, the stretching or vibration peaks associated with phosphorus groups in g-C₃N₄(P) could hardly be observed due to low phosphorus content. This suggests that the original g-C₃N₄ backbone remained almost unchanged after phosphorization in accordance with the above XRD results, proving that the 2D conjugated backbone structures of g-C₃N₄ and g-C₃N₄(P) are well maintained, which is essential for π -delocalized electronic systems to generate and transport photo-excited electron-hole pairs for the subsequent redox reactions [39].

Furthermore, the surface stoichiometry and chemical environment of g-C₃N₄(P) are investigated by XPS measurement. As shown in Fig. 3a,

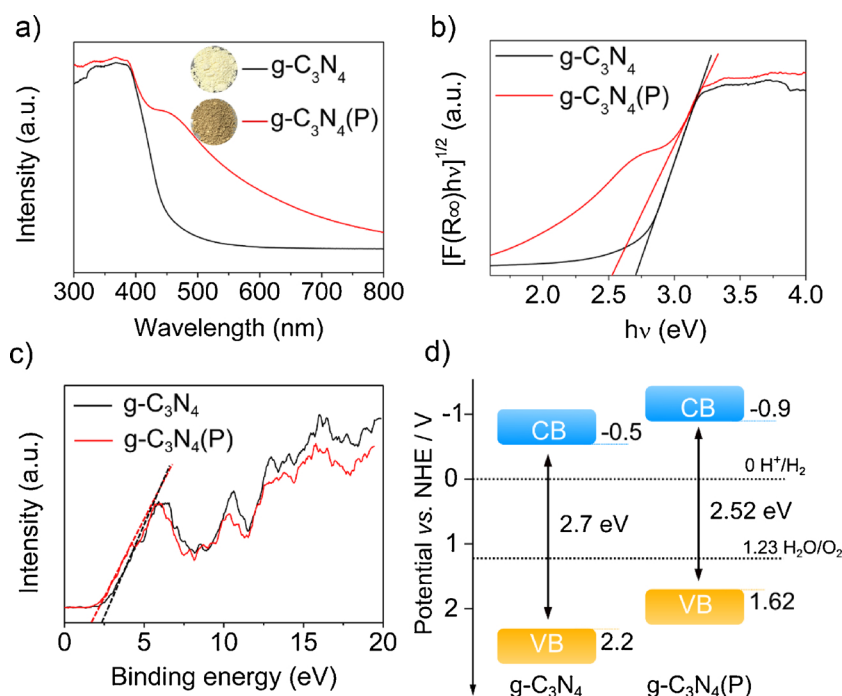


Fig. 1. a) The Uv–vis absorption spectra of g-C₃N₄ and g-C₃N₄(P), the insets are photographs of the corresponding samples. b) The plots of transformed KM function $[F(R_{\infty})h\nu]^{1/2}$ vs. $h\nu$ for g-C₃N₄ and g-C₃N₄(P). c) XPS valence band spectra of g-C₃N₄ and g-C₃N₄(P). d) illustration band structures for g-C₃N₄ and g-C₃N₄(P).

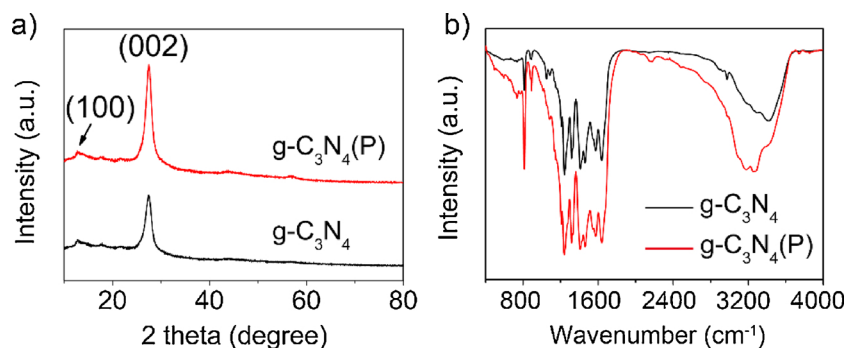


Fig. 2. a) X-ray diffraction patterns and b) FT-IR spectra of g-C₃N₄ and g-C₃N₄(P), respectively.

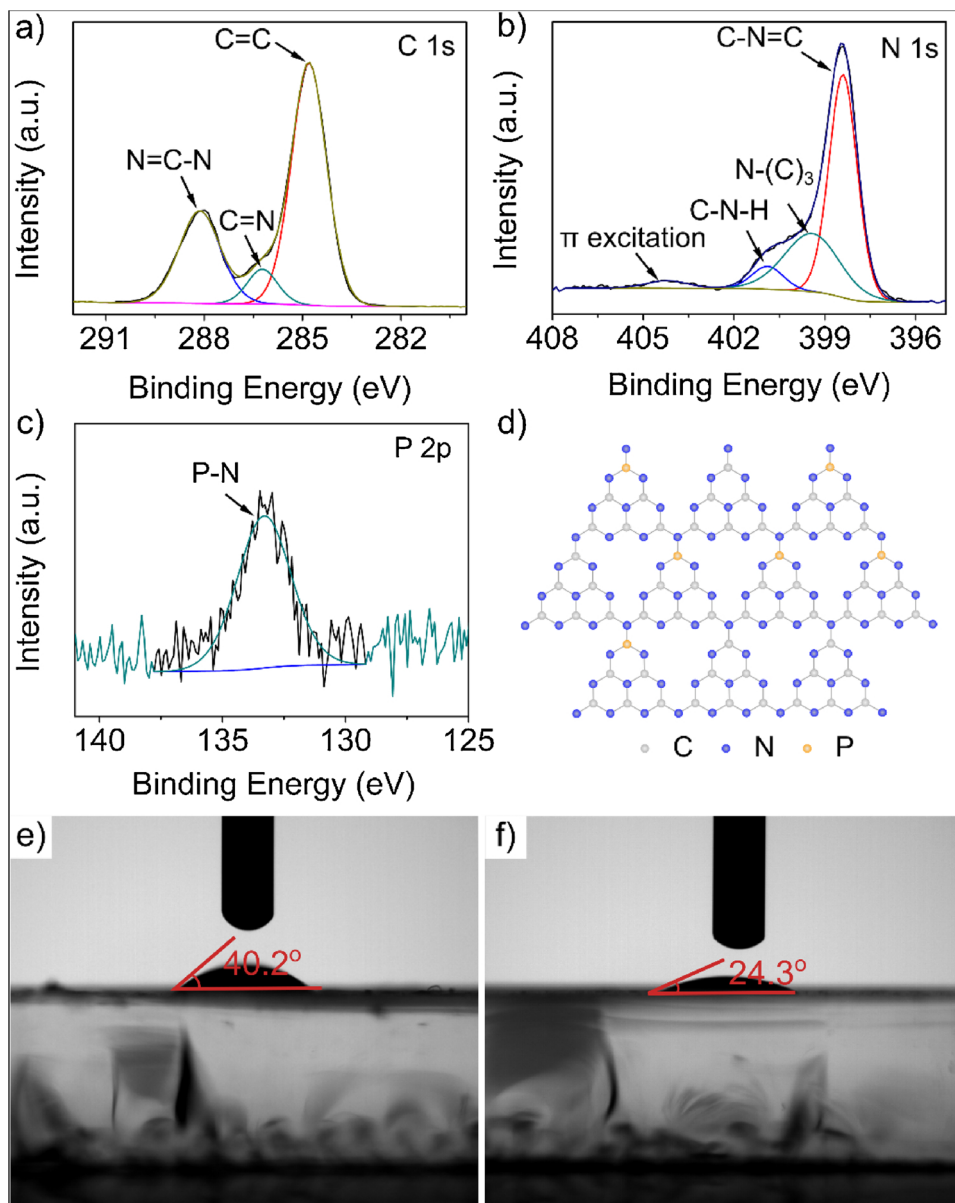


Fig. 3. High-resolution XPS spectra of a) C 1s, b) N 1s and c) P 2p of g-C₃N₄(P), d) an illustration of P atoms randomly replacing some of corner site C atoms in the structure of g-C₃N₄(P) (not representing the precise atom ratio of P atoms to C atoms in g-C₃N₄(P)). Effect of phosphorization on the hydrophilic properties of e) g-C₃N₄ and f) g-C₃N₄(P) thin films as determined by contact angle measurements.

the C 1s spectrum shows three peaks at 284.8 eV, 286.2 eV, and 288.1 eV, which correspond to graphitic carbon (C=C), N–C=N, and sp²-hybridized carbon in the N-containing aromatic ring (N=C–N),

respectively [40,41]. Moreover, N 1s XPS spectrum can be fitted into four N species, i.e., 398.4 eV for sp²-hybridized nitrogen in triazine rings (C–N=C) [42], 399.4 eV for tertiary nitrogen N-(C)₃ groups [43],

400.9 eV for amino functions carrying hydrogen (N–H) [44], and 404.2 eV for π excitation [45], respectively (Fig. 3b). Both C 1s and N 1s XPS spectra confirm the basic heptazine heterocyclic structure of $g\text{-C}_3\text{N}_4$ after phosphorization, corresponding well to XRD and FT-IR results. We also obtain the signal of P 2p XPS spectrum with a P–N bond peak at 133.2 eV (Fig. 3c), which is ($\sim 1\text{--}2$ eV) higher than that of P–C coordination [46]. According to the previous report [39], it is energy-favorable for P heteroatom to replace corner site C atom instead of bay site C atom. Based on the above analysis, we conclude that the P atoms are induced into the framework of $g\text{-C}_3\text{N}_4$ and replace the corner site C atoms to form P–N bonds after the phosphorization treatment. The structure (Fig. 3d) of $g\text{-C}_3\text{N}_4(\text{P})$ is proposed based on this conclusion. There are five valence electrons for P atom, whereas four valence-electrons for C atom. In the framework of $g\text{-C}_3\text{N}_4(\text{P})$, some of the valence electrons of P would participate in the formation of covalent bonds with N neighbors, as evidenced by the XPS spectra of P 2p. Fig. S1 shows the electron paramagnetic resonance (EPR) spectra of $g\text{-C}_3\text{N}_4$ and $g\text{-C}_3\text{N}_4(\text{P})$. Both $g\text{-C}_3\text{N}_4$ and $g\text{-C}_3\text{N}_4(\text{P})$ had one single Lorentzian line with a g value of 2.003, indicating the formation of unpaired electrons on p-conjugated CN aromatic rings [47]. However, the SPR intensity of $g\text{-C}_3\text{N}_4(\text{P})$ are significantly increased compared to that of $g\text{-C}_3\text{N}_4$ due to excessive valence electrons (from P atoms) that are delocalized into the p-conjugated triazine ring to form an electron-rich state

of $g\text{-C}_3\text{N}_4(\text{P})$ [46], resulting in a negatively charged surface which may significantly alter its surface physiochemical properties.

The photocatalytic hydrogen evolution process is a multiphase process referred to the solid (photocatalyst), liquid (reaction solution), and gas phase (hydrogen). It is of great importance to absorb reactant molecule for photocatalyst to undergo the photocatalytic reaction on its surface. Thus, the surface property, especially the hydrophilicity, is very important for $g\text{-C}_3\text{N}_4$. Hence, the effect of phosphorization on the hydrophilic properties of $g\text{-C}_3\text{N}_4(\text{P})$ is studied by measuring the contact angle of these two samples. The contact angle of $g\text{-C}_3\text{N}_4(\text{P})$ is 24.3° (Fig. 3e) which is much smaller than that of $g\text{-C}_3\text{N}_4$ before phosphorization (40.2° , Fig. 3f), suggesting the surface of $g\text{-C}_3\text{N}_4(\text{P})$ is more hydrophilic than that of $g\text{-C}_3\text{N}_4$. This increased hydrophilicity of $g\text{-C}_3\text{N}_4(\text{P})$ is ascribed to the negatively charged surface of $g\text{-C}_3\text{N}_4(\text{P})$ and leads to increase absorption of the reactant molecule in the solution for photocatalytic reaction on its surface.

Both of the $g\text{-C}_3\text{N}_4$ samples before and after phosphorization treatment show a typically stacked lamellar structure with large size and no obvious morphology changes of $g\text{-C}_3\text{N}_4(\text{P})$ are observed after the surface phosphorization treatment (Fig. S2). Transmission electron microscopy (TEM) shows its lamellar nanostructure with curling morphology (Fig. 4a). The corresponding selected area diffraction pattern (Fig. 4a, insert) displays the polycrystalline diffraction rings of the

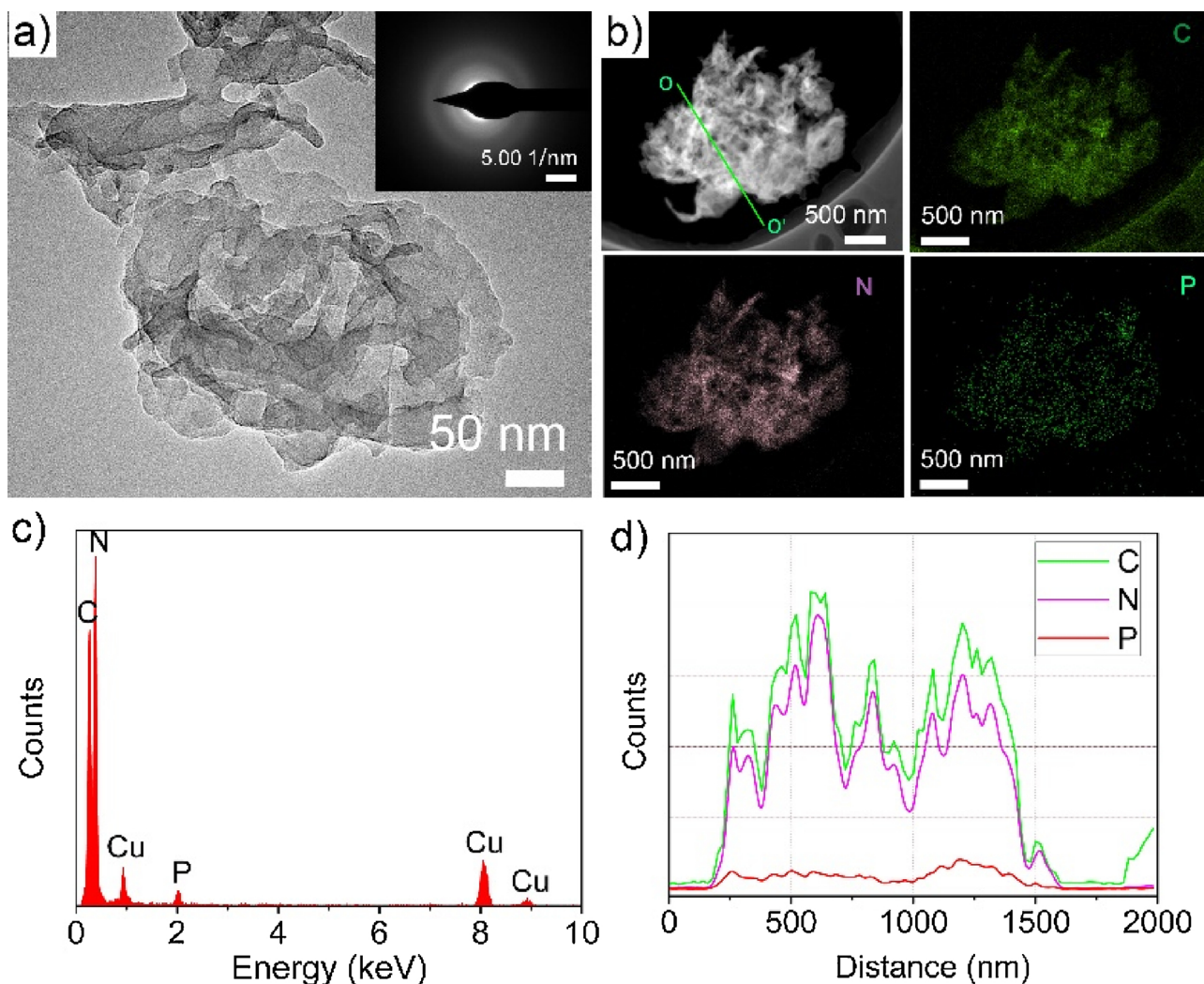


Fig. 4. a) TEM images of $g\text{-C}_3\text{N}_4(\text{P})$, b) High-Angle Annular Dark Field-Scanning Transmission Electron Microscope (HAADF-STEM) image of $g\text{-C}_3\text{N}_4(\text{P})$ and the elemental mapping of C, N, and P, respectively, c) The energy-dispersive X-ray spectra (EDS) recorded from $g\text{-C}_3\text{N}_4(\text{P})$ in b) and d) EDS line scan with C K α , N K α , and P K α signal obtained from the green line in d). The insert in a) is the Selected Area Electron Diffraction (SAED) pattern acquired from a) and the green line (OO') is the track of line scan for the sample in d). (For interpretation of the references to colour in this figure legend, the reader is referred to the web version of this article.)

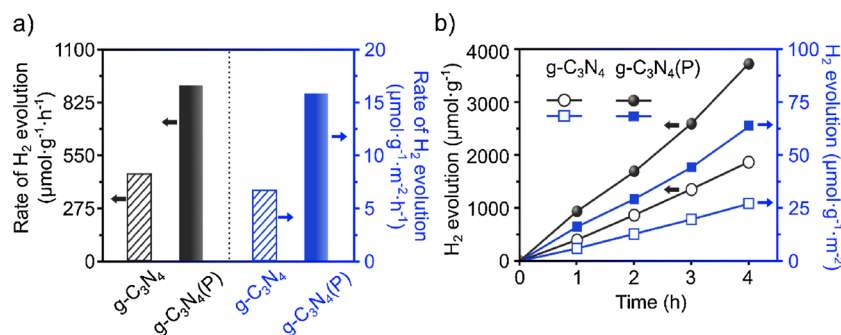


Fig. 5. a) Rates of photocatalytic hydrogen production and b) time-coursed photocatalytic activities over 1 wt% Pt loaded g-C₃N₄ and g-C₃N₄(P). Reaction conditions: 12.5 mg catalyst loaded with 1 wt% Pt; 80 mL aqueous solution containing 10 vol% TEOA, side irradiation Pyrex cell, 300 W Xe lamp.

sample in Fig. 4a, revealing the multicrystalline nature of as-prepared g-C₃N₄(P). Energy-dispersive X-ray spectra (EDS) in Fig. 4b provide a direct evidence of the existence of element P in g-C₃N₄(P) (Fig. 4c). Elemental mapping results demonstrate the C, N, and P elements are homogeneously distributed in the g-C₃N₄(P). The Cu signals in Fig. 4c come from the Cu grid. The EDS spectra in Fig. 4c and line scan profile in Fig. 4d verifies the relatively low concentration of P element in contrast to C and N elements (Fig. 4d, Table S1, 1.53% calculated from EDS and 1.44% measured by ICP-MS). Combined with the results of XPS of g-C₃N₄(P), we conclude that P heteroatoms partially replace the corner site C atoms to form P-N bonds in g-C₃N₄(P) by post thermal phosphorization treatment.

Fig. 5a shows a comparison of hydrogen evolution over g-C₃N₄ and g-C₃N₄(P). The g-C₃N₄(P) sample exhibits a two times higher hydrogen evolution rate of $916.2\ \mu\text{mol}\cdot\text{g}^{-1}\cdot\text{h}^{-1}$ (AOY: 6.52% at 420 nm, Table S3) than g-C₃N₄ ($457.8\ \mu\text{mol}\cdot\text{g}^{-1}\cdot\text{h}^{-1}$ (AQY: 2.55% at 420 nm, Table S3). Moreover, the g-C₃N₄(P) achieves a AQE of 1.48% at 500 nm and 0.7% at 520 nm, respectively (Table S3), revealing the expanded light absorption ($> 500\text{ nm}$) of g-C₃N₄(P) could also contribute to its HER activity. In addition, the BET surface area of g-C₃N₄ and g-C₃N₄(P) are determined to be $58.54\ \text{m}^2/\text{g}$ and $69.21\ \text{m}^2/\text{g}$ (Table S2) by using nitrogen adsorption-desorption method at 77 K (Fig. S3). Thus, the normalized photocatalytic properties are obtained with respect to their specific surface areas and further demonstrate that the activities of the two samples are in the same order of magnitude (Fig. 5a, right). The results are also validated by time-coursed hydrogen production of specific activities (Fig. 5b). As discussed above, with phosphorization treatment, the bandgap of g-C₃N₄ is significantly decreased, the conduction band edge is upshifted, and its hydrophilic surface increases the absorption of reactant molecule for photocatalytic reaction. Moreover, as P atom has more valence electron than C atom, it could act as an electron donor and increase donor density in photocatalyst, leading to the enhanced the charge transfer ability in g-C₃N₄ [48,49]. Therefore,

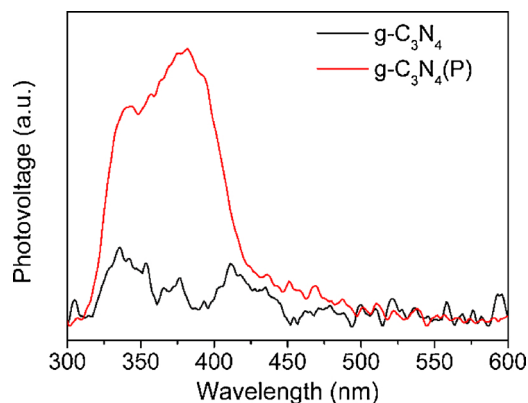


Fig. 6. Surface photovoltage (SPV) spectra of g-C₃N₄ and g-C₃N₄(P).

the superior photocatalytic performance for g-C₃N₄(P) should be reasonably attributed to the extended light absorption, upshifted conduction band edge, enhanced charge transfer, and improved hydrophilic surface by introducing P heteroatom in g-C₃N₄ structure. In addition, the recycling performance and durability of photocatalysts are also of importance from the viewpoint of wide practical applications. To confirm the persistence of the photocatalytic activity of g-C₃N₄(P), cycle experiments of the photocatalytic H₂ generation are carried out by using the same photocatalyst repeatedly for four times under the same conditions. As displayed in Fig. S4, no significant leveling off tendency is observed even with the consecutive 16 h irradiation runs. This result reveals that the g-C₃N₄(P) photocatalyst has remarkable stability for long-term photocatalytic hydrogen production.

SPV measurement (Fig. 6) is used to characterize the separation rate of photogenerated charge carriers over g-C₃N₄ and g-C₃N₄(P). The intensity of the SPV signal reflects the separation rate of the photoinduced electron-hole pairs. Generally, the stronger the responses of SPV spectra, the higher the charge separation [50,51]. The g-C₃N₄ shows little SPV response before phosphorization treatment, while the g-C₃N₄(P) exhibits a dramatically enhanced response, implying an efficient separation of charge carriers in g-C₃N₄(P). Furthermore, the fluorescence spectra of the two samples were recorded to investigate their charge separation efficiency. The intensity of fluorescence for g-C₃N₄(P) was lower than that of g-C₃N₄ (Fig. 5a), indicating that the recombination of photo-induced carriers was dramatically inhibited after the phosphorization treatment. Fig. S5b shows the time-resolved photoluminescence emission decay curves for g-C₃N₄ and g-C₃N₄(P). The reduced average exciton lifetime from 4.641 ns for g-C₃N₄ to 3.746 ns for g-C₃N₄(P) (Fig. S5b, Table S4) indicates that photoexciton dissociation in g-C₃N₄(P) is accelerated in contrast to that in g-C₃N₄ [52,53], revealing the enhanced charge separation in g-C₃N₄(P). As mentioned in the previous discussion, the extra valence electrons of P heteroatom would delocalize into the p-conjugated triazine ring, creating the positive charged P⁺ centers. These P⁺ centers could promote the efficient separation of charge carriers in g-C₃N₄(P) [46].

To better understand the effects of phosphorization on the surface reaction kinetics and hence photocatalytic performances, the linear sweep voltammogram (LSV) of the g-C₃N₄ and g-C₃N₄(P) films are tested in 0.5 M Na₂SO₄ solution containing 20 vol% TEOA at a sweep rate of 10 mV/s, as shown in Fig. 7a. In contrast to g-C₃N₄, the g-C₃N₄(P) shows an anodic shift of ca. 50 mV in hydrogen evolution reaction (HER) onset potential, implying that the HER ability of g-C₃N₄ is improved after phosphorization. Meanwhile, the g-C₃N₄(P) shows a slight of cathodic shift of ca. 10 mV in TEOA oxidation reaction, revealing that the TEOA-oxidation catalytic ability of g-C₃N₄ is also promoted via the phosphorization thermal treatment (Fig. 7b). In addition, electrochemical impedance spectra (EIS) analysis is used to study the charge transfer efficiency on the two samples in the three-electrode system. EIS Nyquist plots of g-C₃N₄ and g-C₃N₄(P) were performed under applied potential at -0.15 V vs. SCE, as shown in

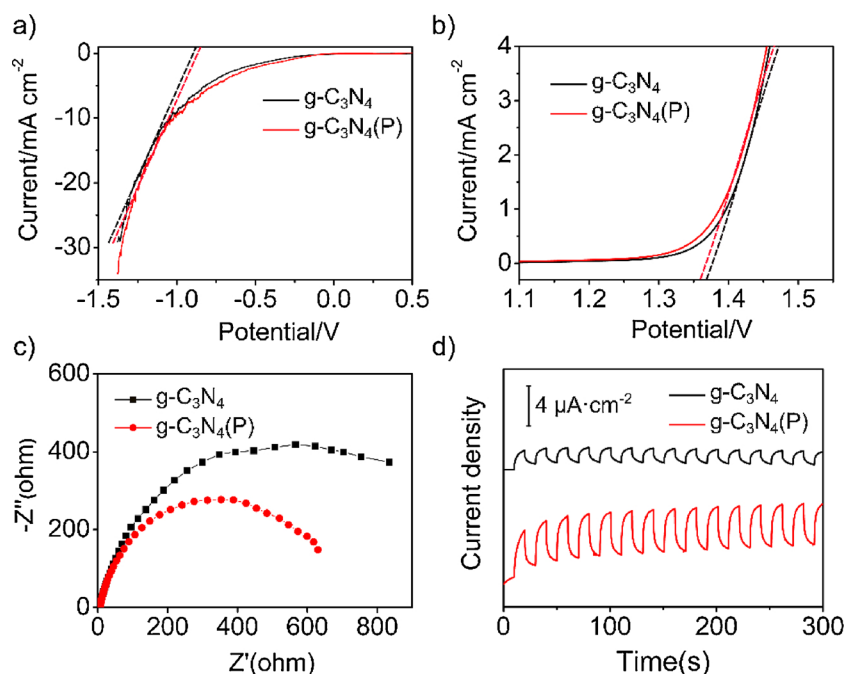


Fig. 7. LSV for a) HER and b) TEOA oxidation reaction of $g\text{-C}_3\text{N}_4$ and $g\text{-C}_3\text{N}_4(\text{P})$ in 0.5 M Na_2SO_4 solution containing 10 vol% TEOA; c) EIS of $g\text{-C}_3\text{N}_4$ and $g\text{-C}_3\text{N}_4(\text{P})$ in 0.5 M Na_2SO_4 solution containing 10 vol% TEOA at -0.15 V vs. SCE; d) Transient photocurrent response of $g\text{-C}_3\text{N}_4$ and $g\text{-C}_3\text{N}_4(\text{P})$ in 0.5 M Na_2SO_4 solution containing 10 vol% TEOA at -0.5 V vs. SCE under simulated solar light.

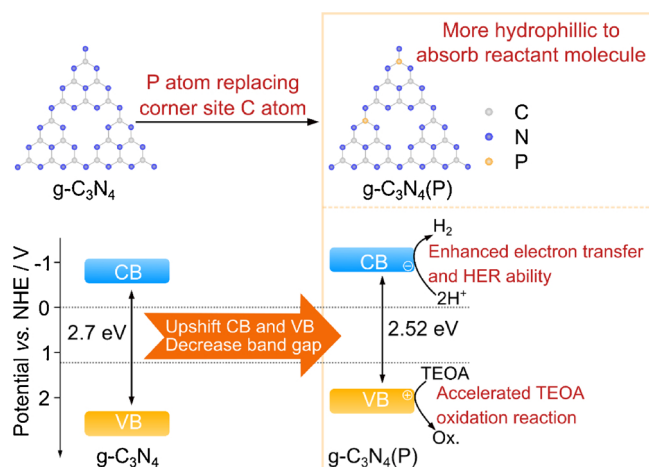


Fig. 8. Photocatalytic hydrogen evolution mechanism of $g\text{-C}_3\text{N}_4$ after phosphorization.

Fig. 7c. The $g\text{-C}_3\text{N}_4(\text{P})$ sample shows an arc with a smaller radius than $g\text{-C}_3\text{N}_4$, revealing an increased charge transfer efficiency at the electrode/electrolyte interface. Furthermore, we compare the transient photocurrent responses of the $g\text{-C}_3\text{N}_4$ and $g\text{-C}_3\text{N}_4(\text{P})$ films. The photocurrent density of $g\text{-C}_3\text{N}_4(\text{P})$ is ca. 3 times higher than that of $g\text{-C}_3\text{N}_4$ (Fig. 7d), corresponding to the enhancement in photocatalytic activities for $g\text{-C}_3\text{N}_4(\text{P})$ as compared to $g\text{-C}_3\text{N}_4$.

Based on the above analysis, the mechanism of enhanced photocatalytic hydrogen evolution of $g\text{-C}_3\text{N}_4$ after phosphorization is illustrated in Fig. 8. First, the phosphorization treatment introduces P heteroatoms into the framework of $g\text{-C}_3\text{N}_4$ and P atoms replaces the corner site C atoms forming P-N bonds. The excess valence electrons of P lead to the negatively charged surface of $g\text{-C}_3\text{N}_4$, resulting in the increased surface hydrophilicity and absorption of reactant molecule for photocatalytic reaction. Secondly, by phosphorization treatment, the band gap of $g\text{-C}_3\text{N}_4$ decreases and its light absorption is extended up to ~ 650 nm, enhancing the ability to generate photo-induced electron-hole pairs for photocatalytic reaction. After phosphorization, the conduction band edge of $g\text{-C}_3\text{N}_4$ is upshifted, leading to a

thermodynamically favorable photocatalytic hydrogen reaction. Thirdly, charge transfer ability in $g\text{-C}_3\text{N}_4(\text{P})$ is improved due to the increased donor density, which is caused by the induced P heteroatom. Last, the enhanced HER and TEOA-oxidation catalytic abilities of $g\text{-C}_3\text{N}_4$ by phosphorization thermal treatment further increase the efficiency of photocatalysis reaction. Therefore, the $g\text{-C}_3\text{N}_4$ after phosphorization treatment shows higher photocatalytic hydrogen evolution activity than the pristine one.

4. Conclusions

In summary, we successfully modified the atom structure of $g\text{-C}_3\text{N}_4$ by partially replacing corner site C atom with P heteroatoms in the network of $g\text{-C}_3\text{N}_4$ via a simple thermal phosphorization treatment, and significantly altered the band structure, surface property, and surface catalytic ability for hydrogen evolution. First, the bandgap of $g\text{-C}_3\text{N}_4$ after phosphorization dramatically decreased and the conduction band edge upshifted, leading to the extended light absorption and more energetic photo-induced electrons for HER. Secondly, the hydrophilic surface of $g\text{-C}_3\text{N}_4$ after phosphorization increased the absorption of reactant molecule for photocatalytic reaction due to the negative charge surface caused by excess valence electrons of P heteroatom. Last, the HER ability and TEOA-oxidation catalytic ability of $g\text{-C}_3\text{N}_4$ with phosphorization treatment were promoted. Therefore, the $g\text{-C}_3\text{N}_4$ by thermal phosphorization treatments showed higher photocatalytic hydrogen evolution activity when compared with the pristine one. This work provides a simple approach to modifying the structure of $g\text{-C}_3\text{N}_4$, which could also be applied to other semiconductors for designing photocatalyst with unique structure and high activity.

Notes

The authors declare no competing financial interest.

Acknowledgments

The authors gratefully acknowledge financial support from the China Scholarship Council. This work is supported by China Postdoctoral Science Foundation (No. 2017M623161), National Natural Science Foundation of China (No. 51802255), the China Fundamental

Research Funds for the Central Universities, the World-Class Universities (Disciplines) and the Characteristic Development Guidance Funds for the Central Universities, and the U.S. Department of Energy (DOE), Office of Science, Office of Basic Energy Sciences, Early Career Research program under Award #67037. We thank the support from the Instrument Analysis Center of Xi'an Jiaotong University.

Appendix A. Supplementary data

Supplementary data associated with this article can be found, in the online version, at <https://doi.org/10.1016/j.apcatb.2018.10.044>.

References

- [1] I. Roger, M.A. Shipman, M.D. Symes, *Nat. Rev. Chem.* 1 (2017) 0003.
- [2] J.H. Montoya, L.C. Seitz, P. Chakthranont, A. Vojvodic, T.F. Jaramillo, J.K. Nørskov, *Nature Mater.* 16 (2016) 70.
- [3] B. Wang, M. Liu, Z. Zhou, L. Guo, *Adv. Sci.* 2 (2015) 1500153.
- [4] M. Ge, Q. Li, C. Cao, J. Huang, S. Li, S. Zhang, Z. Chen, K. Zhang, S.S. Al-Deyab, Y. Lai, *Adv. Sci.* 4 (2017) 1600152.
- [5] B. Wang, S. Shen, S.S. Mao, *J. Materiomics* 3 (2017) 96–111.
- [6] W.-J. Ong, L.-L. Tan, Y.H. Ng, S.-T. Yong, S.-P. Chai, *Chem. Rev.* 116 (2016) 7159–7329.
- [7] J. Xu, M. Shalom, *ACS Appl. Mater. Interfaces* 8 (2016) 13058–13063.
- [8] B. Wang, S. Shen, L. Guo, *Appl. Catal. B: Environ.* 166–167 (2015) 320–326.
- [9] B. Kurpil, B. Kumru, T. Heil, M. Antonietti, A. Savateev, *Green Chem.* 20 (2018) 838–842.
- [10] A. Savateev, B. Kurpil, A. Mishchenko, G. Zhang, M. Antonietti, *Chem. Sci.* 9 (2018) 3584–3591.
- [11] B. Kurpil, K. Otte, M. Antonietti, A. Savateev, *Appl. Catal. B: Environ.* 228 (2018) 97–102.
- [12] J. Barrio, L. Lin, X. Wang, M. Shalom, *ACS Sustainable Chem. Eng.* 6 (2018) 519–530.
- [13] L. Lin, W. Ren, C. Wang, A.M. Asiri, J. Zhang, X. Wang, *Appl. Catal. B: Environ.* 231 (2018) 234–241.
- [14] W.-J. Ong, *Front. Mater.* 4 (2017).
- [15] W.-J. Ong, L.K. Putri, Y.-C. Tan, L.-L. Tan, N. Li, Y.H. Ng, X. Wen, S.-P. Chai, *Nano Res.* 10 (2017) 1673–1696.
- [16] D. Zeng, W.-J. Ong, Y. Chen, S.Y. Tee, C.S. Chua, D.-L. Peng, M.-Y. Han, *Part. Part. Syst. Charact.* 35 (2018) 1700251.
- [17] D. Zeng, W. Xu, W.-J. Ong, J. Xu, H. Ren, Y. Chen, H. Zheng, D.-L. Peng, *Appl. Catal. B: Environ.* 221 (2018) 47–55.
- [18] D. Zeng, P. Wu, W.-J. Ong, B. Tang, M. Wu, H. Zheng, Y. Chen, D.-L. Peng, *Appl. Catal. B: Environ.* 233 (2018) 26–34.
- [19] B. Kurpil, A. Savateev, V. Papaefthimiou, S. Zafeiratos, T. Heil, S. Özenler, D. Dontsova, M. Antonietti, *Appl. Catal. B: Environ.* 217 (2017) 622–628.
- [20] L. Li, D. Cruz, A. Savateev, G. Zhang, M. Antonietti, Y. Zhao, *Appl. Catal. B: Environ.* 229 (2018) 249–253.
- [21] A. Savateev, S. Pronkin, J.D. Epping, M.G. Willinger, M. Antonietti, D. Dontsova, *J. Mater. Chem. A* 5 (2017) 8394–8401.
- [22] X. Wang, X. Chen, A. Thomas, X. Fu, M. Antonietti, *Adv. Mater.* 21 (2009) 1609–1612.
- [23] W. Zhang, J. Barrio, C. Gervais, A. Kocjan, A. Yu, X. Wang, M. Shalom, *Angew. Chem. Int. Ed.* 57 (2018) 9764–9769.
- [24] Z.-F. Huang, J. Song, L. Pan, Z. Wang, X. Zhang, J.-J. Zou, W. Mi, X. Zhang, L. Wang, *Nano Energy* 12 (2015) 646–656.
- [25] G. Dong, K. Zhao, L. Zhang, *Chem. Commun.* 48 (2012) 6178–6180.
- [26] P. Niu, L.C. Yin, Y.Q. Yang, G. Liu, H.M. Cheng, *Adv. Mater.* 26 (2014) 8046–8052.
- [27] M. Zhou, Z. Hou, X. Chen, *Part. Part. Syst. Charact.* 35 (2018) 1700038.
- [28] X.L. Wang, W.Q. Fang, W. Liu, Y. Jia, D. Jing, Y. Wang, L.-Y. Yang, X.-Q. Gong, Y.-F. Yao, H.G. Yang, X. Yao, *J. Mater. Chem. A* 5 (2017) 19227–19236.
- [29] Y. Hou, A.B. Laursen, J. Zhang, G. Zhang, Y. Zhu, X. Wang, S. Dahl, I. Chorkendorff, *Angew. Chem. Int. Ed.* 52 (2013) 3621–3625.
- [30] Y. Hou, Y. Zhu, Y. Xu, X. Wang, *Appl. Catal. B: Environ.* 156–157 (2014) 122–127.
- [31] Q. Liang, Z. Li, Z.H. Huang, F. Kang, Q.H. Yang, *Adv. Funct. Mater.* 25 (2015) 6885–6892.
- [32] P. Yang, J. Zhao, W. Qiao, L. Li, Z. Zhu, *Nanoscale* 7 (2015) 18887–18890.
- [33] Y. Cao, Z. Zhang, J. Long, J. Liang, H. Lin, H. Lin, X. Wang, *J. Mater. Chem. A* 2 (2014) 17797–17807.
- [34] G. Liu, P. Niu, C. Sun, S.C. Smith, Z. Chen, G.Q. Lu, H.-M. Cheng, *J. Am. Chem. Soc.* 132 (2010) 11642–11648.
- [35] Y. Cui, G. Zhang, Z. Lin, X. Wang, *Appl. Catal. B: Environ.* 181 (2016) 413–419.
- [36] M. Sun, H. Liu, J. Qu, J. Li, *Adv. Energy Mater.* 6 (2016) 1600087.
- [37] V. Kumar, S. Kr. Sharma, T.P. Sharma, V. Singh, *Opt. Mater.* 12 (1999) 115–119.
- [38] S. Kang, W. Huang, L. Zhang, M. He, S. Xu, D. Sun, X. Jiang, *ACS Appl. Mater. Interfaces* 10 (2018) 13796–13804.
- [39] J. Ran, T.Y. Ma, G. Gao, X.-W. Du, S.Z. Qiao, *Energy Environ. Sci.* 8 (2015) 3708–3717.
- [40] S. Zhao, Z. Tang, S. Guo, M. Han, C. Zhu, Y. Zhou, L. Bai, J. Gao, H. Huang, Y. Li, Y. Liu, Z. Kang, *ACS Catal.* 8 (2018) 188–197.
- [41] Y. Zhang, S. Zong, C. Cheng, J. Shi, P. Guo, X. Guan, B. Luo, S. Shen, L. Guo, *Appl. Catal. B: Environ.* 233 (2018) 80–87.
- [42] S. Guo, Z. Deng, M. Li, B. Jiang, C. Tian, Q. Pan, H. Fu, *Angew. Chem. Int. Ed.* 55 (2016) 1830–1834.
- [43] Q. Liang, Z. Li, X. Yu, Z.H. Huang, F. Kang, Q.H. Yang, *Adv. Mater.* 27 (2015) 4634–4639.
- [44] Y. Zeng, C. Liu, L. Wang, S. Zhang, Y. Ding, Y. Xu, Y. Liu, S. Luo, *J. Mater. Chem. A* 4 (2016) 19003–19010.
- [45] J. Liu, T. Zhang, Z. Wang, G. Dawson, W. Chen, *J. Mater. Chem.* 21 (2011) 14398–14401.
- [46] Y. Zhou, L. Zhang, J. Liu, X. Fan, B. Wang, M. Wang, W. Ren, J. Wang, M. Li, J. Shi, *J. Mater. Chem. A* 3 (2015) 3862–3867.
- [47] J. Zhang, X. Chen, K. Takanabe, K. Maeda, K. Domen, J.D. Epping, X. Fu, M. Antonietti, X. Wang, *Angew. Chem. Int. Ed.* 49 (2010) 441–444.
- [48] G. Wang, H. Wang, Y. Ling, Y. Tang, X. Yang, R.C. Fitzmorris, C. Wang, J.Z. Zhang, Y. Li, *Nano Lett.* 11 (2011) 3026–3033.
- [49] B. Wang, S. Shen, L. Guo, *ChemCatChem* 8 (2016) 798–804.
- [50] J. Li, X. Zhang, F. Raziq, J. Wang, C. Liu, Y. Liu, J. Sun, R. Yan, B. Qu, C. Qin, L. Jing, *Appl. Catal. B: Environ.* 218 (2017) 60–67.
- [51] G. Bian, P. Jiang, F. Wang, Y. Shen, K. Jiang, L. Liu, W. Zhang, *New J. Chem.* 42 (2018) 85–90.
- [52] Y. Cao, S. Chen, Q. Luo, H. Yan, Y. Lin, W. Liu, L. Cao, J. Lu, J. Yang, T. Yao, S. Wei, *Angew. Chem. Int. Ed.* 129 (2017) 12359–12364.
- [53] W. Liu, L. Cao, W. Cheng, Y. Cao, X. Liu, W. Zhang, X. Mou, L. Jin, X. Zheng, W. Che, Q. Liu, T. Yao, S. Wei, *Angew. Chem. Int. Ed.* 129 (2017) 9440–9445.